A finite element formulation to identify damage fields: The equilibrium gap method

Damien Claire, François Hild, Stéphane Roux

A Finite Element Formulation to Identify Damage Fields: The equilibrium gap method

D. Claire,[1,2] F. Hild[1,*] and S. Roux[2]

[1] *LMT-Cachan, ENS de Cachan / CNRS-UMR 8535 / Université Paris 6*
61 avenue du Président Wilson, F-94235 Cachan Cedex, France.
[2] *Laboratoire "Surface du Verre et Interfaces", UMR CNRS/Saint-Gobain 125*
39 quai Lucien Lefranc, F-93303 Aubervilliers Cedex, France.

SUMMARY

It is proposed to determine damage parameters in two dimensions (surface of a material) or three dimensions (in the bulk of a solid) by using full-field displacement measurements. A finite-element approach is developed to evaluate piece-wise constant elastic parameters modeled by an isotropic damage variable. Two sets of examples are discussed. The first series deals with mechanical fields obtained by finite element simulations to assess the performance of the approach. The second series is concerned with displacement measurements performed during a biaxial test on a composite material.

KEY WORDS: Continuum Damage Mechanics/ identification/ inverse problem/ full-field measurements

*Correspondence to: LMT-Cachan, ENS de Cachan / CNRS-UMR 8535 / Université Paris 6
61 avenue du Président Wilson, F-94235 Cachan Cedex, France.
Email: francois.hild@lmt.ens-cachan.fr

Contract/grant sponsor: This work was supported by CNRS in a project entitled "Analyses multi-échelles de champs de déformation par traitement d'image : vers l'identification de champs de propriétés mécaniques."

1. INTRODUCTION

The current development of reliable displacement field measurement techniques enables one to better characterize the behavior of materials and the response of structures to external loadings. Homogeneous materials under complex load histories or heterogeneous microstructures induce kinematic fields that require full-field analyses to understand the interactions between the material microstructure and the external loading. To bridge the gap between experiments and numerical simulations, full-field measurement techniques and model identification can be utilized.

Among different measurement techniques [1, 2, 3, 4, 5], digital image correlation is one of the most appealing in solid mechanics. It is fast, sensitive and versatile so that sub-minute runs on conventional PCs give access to displacement fields with more than 1000 measurement "points". The rapid development of reasonably cheap CCD cameras allows the user to acquire good quality images (namely, high pixel count, large dynamic range) and achieve sub-pixel resolution that are needed in many applications [6]. For instance, the possibility to resolve strain heterogeneities, and thus to determine complete displacement maps becomes highly desirable (*e.g.,* experiments on heterogeneous materials [3], detection of crack initiation [7] or strain singularities [8], and analysis of strain localization [9]).

Full-field measurements often need inversion techniques to determine the mechanical properties field of the materials. Updating techniques based upon the constitutive equation error [10, 11, 12] have been used in the analysis of vibrations [13], the determination of damage fields [14] or to study heterogeneous tests (*e.g.,* Brazilian test [15]). An alternative to the previous approach is, for instance, the so-called virtual field method that has been used to identify homogeneous properties of composites [16, 17] (*i.e.,* in anisotropic elasticity). Another procedure is based upon the reciprocity gap [18] that can also be used to determine the local elastic field or to detect cracks in elastic media [19].

In this paper, we propose another method that only needs displacement field data. In the

present case, the in-plane displacements are measured on surfaces of samples by digital image correlation. It therefore consists in identifying elastic property fields on the surface of a sample. The practical applications discussed herein are restricted to plane stress hypotheses. However, with the use, for instance, of X-Ray (micro)tomography [20], 3D maps of density variations can be reconstructed. A full 3D displacement field is therefore measurable by correlating density maps at different stages of an experiment and the same identification procedure may be applicable to these situations. Section 2 is devoted to the discussion of continuum and discrete formulations of the problem. In Section 3, the implementation is discussed when a piece-wise constant property field is sought. A non-conventional finite element formulation is derived, which is consistent with the available information (*i.e.,* the measured displacement field). Different error indicators are introduced in Section 4. Section 5 deals with cases where the input data (*i.e.,* displacement field) is obtained via a classical FE computation. Its role is to assess the intrinsic properties of the identification procedure when dealing with uniform, layered or random damage fields. In Section 6, a heterogeneous test is analyzed and the conditions for crack inception are examined by using an isotropic description of damage.

2. MECHANICAL ANALYSIS

In the following, an identification formulation is derived in which the displacements $\boldsymbol{u}(\boldsymbol{x})$ are *known* and the elastic properties are unknown. This problem setting is unconventional in the sense that classical FE formulations assume known mechanical properties and try to determine the displacement field for different types of boundary conditions.

2.1. Continuum Case

Let us consider a structure Ω. In the absence of body forces, equilibrium is described by

$$\mathbf{div}[\boldsymbol{\sigma}(\boldsymbol{u})] = \mathbf{0}, \tag{1}$$

where $\boldsymbol{\sigma}$ is the Cauchy stress tensor that depends on the known displacement $\boldsymbol{u}$. In the sequel, the heterogeneity of the elastic field is reduced to a scalar and isotropic damage field $D(\boldsymbol{x})$ [21]. For this type of damage description, the Poisson's ratio is unaffected and the Lamé's coefficients can be written as $\lambda(\boldsymbol{x}) = \lambda_0[1 - D(\boldsymbol{x})]$ and $\mu(\boldsymbol{x}) = \mu_0[1 - D(\boldsymbol{x})]$, where the subscript $_0$ refers to reference quantities. In this case, when $D(\boldsymbol{x})$ is less than 1, Eqn. (1) becomes

$$[2\mu_0\boldsymbol{\epsilon}(\boldsymbol{u}) + \lambda_0 \mathrm{tr}\{\boldsymbol{\epsilon}(\boldsymbol{u})\}\mathbf{1}]\,\mathbf{grad}[\ln(1-D)] + \mathbf{div}[2\mu_0\boldsymbol{\epsilon}(\boldsymbol{u}) + \lambda_0 \mathrm{tr}\{\boldsymbol{\epsilon}(\boldsymbol{u})\}\mathbf{1}] = \mathbf{0}, \tag{2}$$

where $\boldsymbol{\epsilon}(\boldsymbol{u})$ is the infinitesimal strain tensor. By introducing the *bare* stress field, $\boldsymbol{\Sigma}(\boldsymbol{u}) = 2\mu_0\boldsymbol{\epsilon}(\boldsymbol{u}) + \lambda_0 \mathrm{tr}\{\boldsymbol{\epsilon}(\boldsymbol{u})\}\mathbf{1}$ as if $D = 0$, the above equation can be written as

$$\boldsymbol{\Sigma}(\boldsymbol{u})\mathbf{grad}[\ln(1-D)] + \mathbf{div}[\boldsymbol{\Sigma}(\boldsymbol{u})] = \mathbf{0} \tag{3}$$

and hence, in a generic case where $\det[\boldsymbol{\Sigma}(\boldsymbol{u})] \neq 0$, the above relation can be inverted to give

$$\mathbf{grad}[\ln(1-D)] = -\boldsymbol{\Sigma}^{-1}(\boldsymbol{u})\mathbf{div}[\boldsymbol{\Sigma}(\boldsymbol{u})]. \tag{4}$$

Let us note from this expression that, starting from an estimate of the displacement field $\boldsymbol{u}$ from which $\boldsymbol{\epsilon}(\boldsymbol{u})$ and then $\boldsymbol{\Sigma}(\boldsymbol{u})$ are computed, it is not guaranteed that the r.h.s. of Eqn. (4) derives from a scalar field $\ln(1-D)$. A necessary and sufficient condition for the existence of such a field is that

$$\mathbf{curl}\left\{\boldsymbol{\Sigma}^{-1}(\boldsymbol{u})\mathbf{div}[\boldsymbol{\Sigma}(\boldsymbol{u})]\right\} = \mathbf{0}. \tag{5}$$

Equation (5) is a compatibility condition comparable to the classical Beltrami kinematic compatibility condition. Therefore, the information provided by the displacement field is redundant. There exist also cases where Eqn. (2) cannot be inverted to determine $\mathbf{grad}[\ln(1-D)]$. It corresponds to cases where (at least) one eigenvalue of the bare stress tensor is 0. However, in generic cases, this condition will apply only at discrete points, or along a free boundary. The former case can be handled easily, because of the isolated nature of these points. The latter is a priori more difficult, however, even though the component of $\mathbf{grad}[\ln(1-D)]$

normal to the free surface cannot be determined, the tangential component may be sufficient to have access to $1-D$. Thus, along such a boundary, the above equation is no longer redundant, and it may be a signal calling attention to the fact that the determination of damage close to a free surface may be less accurate than the bulk determination.

It may also be noted that the redundant character of this equation results from the assumption of a *single* isotropic scalar damage parameter. If for instance, λ and μ were experiencing variations from places to places, without a fixed ratio as in the present problem, the redundant nature of the equation is lost, but the problem is still solvable (*i.e.,* well-posed) at least by sub-domains separated by curves through which jumps in the elastic constants could exist [22]. In the latter case, the well-posedness could re-emerge if one takes into account an extraneous condition such as the smooth variation in the elastic constants (what may or may not be legitimate). This subtle question is however irrelevant for the case of an isotropic scalar damage field. Thus the compatibility equations can be used as a measure of the soundness of the initial hypotheses, and provided they are satisfied, the damage field can be estimated by integration of the gradient field. We also note that because no information on the loading is incorporated in the present formulation, the $(1-D)$-field is determined up to a multiplicative constant.

Lastly, an approximate evaluation of the damage field $\hat{D}$ leads to the existence of body force residuals $\boldsymbol{f}_r$

$$\boldsymbol{f}_r(\hat{D}) = [2\mu_0\boldsymbol{\epsilon}(\boldsymbol{u}) + \lambda_0 \mathrm{tr}\{\boldsymbol{\epsilon}(\boldsymbol{u})\}\mathbf{1}]\,\mathbf{grad}[\ln(1-\hat{D})] + \mathbf{div}[2\mu_0\boldsymbol{\epsilon}(\boldsymbol{u}) + \lambda_0 \mathrm{tr}\{\boldsymbol{\epsilon}(\boldsymbol{u})\}\mathbf{1}], \quad (6)$$

so that a weak form of an identification procedure of a damage field would lead to the minimization of the body force residuals over a given domain Ω

$$\min \|\boldsymbol{f}_r(\hat{D})\|_\Omega^2 \quad (7)$$

where $\|.\|_\Omega$ denotes any suitable norm taken over a domain Ω (*e.g.,* an "energy norm"). Consequently, the present procedure is referred to as equilibrium gap method.

2.2. Discontinuous Case

The previous analysis is valid for continuous and differentiable property (*i.e.,* damage) fields. When the considered medium is assumed to have damage discontinuities, a more suitable setting is needed, *i.e.,* Eqn. (1) now corresponds to a continuity of the stress vector across a surface of normal $\boldsymbol{n}$

$$[\![\boldsymbol{\sigma}.\boldsymbol{n}]\!] = \mathbf{0}, \tag{8}$$

where $[\![\star]\!]$ denotes the jump of the quantity $\star$. For a normal $\boldsymbol{n} = \boldsymbol{e}_x$, under plane strain conditions, Eqn. (8) becomes

$$[\![(1-D)\{\lambda_0(\varepsilon_{xx}+\varepsilon_{yy})+2\mu_0\varepsilon_{xx}\}]\!] = 0, \;\; [\![(1-D)\mu_0\varepsilon_{xy}]\!] = 0, \tag{9}$$

(the corresponding plane stress condition could be written in similar terms). As mentioned earlier, the evaluation of the field $(1-D)$ is obtained up to a multiplicative constant, since no force measures are considered.

2.3. FE Approach

The jump conditions (9) are directly applied to a FE formulation. Contrary to classical settings, the nodal displacements are *inputs* whereas elastic coefficients are *unknown.* The potential energy theorem allows for a weak formulation of the equilibrium equations (1), which is linearly dependent on the displacements *and* elastic properties. Since most measurement techniques yield data on a regular mesh of points, the same hypothesis is made for the identification procedure. Consequently, quadratic square elements are considered for which each node corresponds to a measurement point. This hypothesis allows us to derive a specific formulation in which only middle nodes are considered. When the damage parameter D_e is constant for a given element e occupying a domain Ω_e, the elementary stiffness matrix can be written as

$$[\boldsymbol{K}_{me}](D_e) = (1 - D_e)[\boldsymbol{K}_{me0}] \tag{10}$$

where $[\boldsymbol{K}_{me0}]$ is the elementary stiffness matrix of an undamaged element. Similarly, the strain energy E_{me} can be written as

$$E_{me}(D_e, \{\boldsymbol{u}_e\}) = \frac{1 - D_e}{2} \{\boldsymbol{u}_e\}^t [\boldsymbol{K}_{me0}] \{\boldsymbol{u}_e\}, \tag{11}$$

where $\{\boldsymbol{u}_e\}$ is the nodal displacement column vector and ^{t} the matrix transposition. In the absence of external load on the considered nodes, the equilibrium conditions (8) can be rewritten for each middle node '$\pm$' of two neighboring elements '$-$' and '$+$'

$$\frac{\partial E_{m\pm}}{\partial \boldsymbol{u}_\pm}(D_e^-, D_e^+, \{\boldsymbol{u}_e^-\} = \{\boldsymbol{u}_m^-\}, \{\boldsymbol{u}_e^+\} = \{\boldsymbol{u}_m^+\}) = \boldsymbol{0}, \tag{12}$$

with

$$E_{m\pm}(D_e^-, D_e^+, \{\boldsymbol{u}_e^-\}, \{\boldsymbol{u}_e^+\}) = E_{me}(D_e^-, \{\boldsymbol{u}_e^-\}) + E_{me}(D_e^+, \{\boldsymbol{u}_e^+\}), \tag{13}$$

where $\boldsymbol{u}_\pm$ is the displacement vector of the considered middle node '$\pm$', D_e^-, D_e^+ are the damage variables in elements '$-$' and '$+$', respectively. In Eqn. (12), the equilibrium condition is written when the nodal displacements $\{\boldsymbol{u}_e^-\}$ and $\{\boldsymbol{u}_e^+\}$ are equal to the corresponding measurements $\{\boldsymbol{u}_m^-\}$ and $\{\boldsymbol{u}_m^+\}$. By considering this condition for each middle node, one ends up with a linear system in which the unknowns are the damage parameters assumed to be piece-wise constant and the known quantities are all the measured nodal displacements. If Eqn. (12) is not strictly satisfied, then a residual force $\boldsymbol{F}_r$ arises

$$\boldsymbol{F}_r(\hat{D}_e^-, \hat{D}_e^+, \{\boldsymbol{u}_m^-\}, \{\boldsymbol{u}_m^+\}) = \frac{\partial E_m}{\partial \boldsymbol{u}_\pm}(\hat{D}_e^-, \{\boldsymbol{u}_m^-\}) + \frac{\partial E_m}{\partial \boldsymbol{u}_\pm}(\hat{D}_e^+, \{\boldsymbol{u}_m^+\}), \tag{14}$$

where $\hat{D}_e^-$ and $\hat{D}_e^+$ are trial values of the unknown damage variables. The aim of the following section is to propose a practical setting for the identification of a damage field from the knowledge of displacement fields by minimizing the residuals $\boldsymbol{F}_r$.

It is worth mentioning that the present approach is close, in its initial setting (*i.e.,* based on weak equilibrium conditions), to the virtual field method [16]. In the present case, the shape function associated to middle nodes of finite elements corresponds to a particular choice of the trial (or virtual) displacement field. However, the input is the measured *displacement* field as opposed to the strain field needed in the virtual field method and the constitutive equation error approach [14]. It can be noted that the latter can also use displacement fields [15].

3. PRACTICAL FORMULATION

Since damage is assumed to be isotropic, a more appropriate setting can be used. The k^{th} equilibrium condition becomes

$$\bar{g}_k(\{\boldsymbol{u}_m^-\})(1-D_e^-) = \breve{g}_k(\{\boldsymbol{u}_m^+\})(1-D_e^+), \tag{15}$$

where $\bar{g}$ and $\breve{g}$ are generic functions depending on the nodal displacements (see Appendix A). By considering all the equilibrium equations, the following global system is obtained

$$[\boldsymbol{G}]\{\boldsymbol{D}\} = \{\boldsymbol{g}\} \quad \text{with} \quad \{\boldsymbol{D}\}^t = \{D_1\ D_2\ \ldots\ D_N\}\,, \tag{16}$$

where $[\boldsymbol{G}]$ and $\{\boldsymbol{g}\}$ are known and contain the nodal displacements. The advantage of this setting is that it can be written in a logarithmic form

$$\ln(1-D_e^-) - \ln(1-D_e^+) = \ln|\breve{g}_k(\{\boldsymbol{u}_m^-\})| - \ln|\bar{g}_k(\{\boldsymbol{u}_m^+\})|. \tag{17}$$

Equation (17) automatically satisfies the requirement $D < 1$. However, this type of formulation can only be used for middle points. When corner nodes are concerned with (generally) four damage unknowns associated to the connecting elements, the same logarithmic form [Eqn. (17)] cannot be used. However, the original setting corresponding to the equilibrium condition [Eqn. (12)] can be written for corner nodes and would also lead to a *linear* system similar to Eqn. (15) generally containing four unknowns per equation.

The system to solve is

$$[\boldsymbol{M}]\{\boldsymbol{d}\} = \{\boldsymbol{q}\}, \tag{18}$$

where $\{\boldsymbol{d}\}$ is defined by

$$\{\boldsymbol{d}\}^t = \{\ln(1-D_1)\ \ln(1-D_2)\ \ldots\ \ln(1-D_N)\}, \tag{19}$$

$[\boldsymbol{M}]$ an assembled matrix corresponding to all the conditions (17) and only depends on the topology of the mesh (*i.e.,* it is independent of the displacement measurements) whereas $\{\boldsymbol{q}\}$ is a vector that depends upon the measured displacements.

At this level, we can make the connection with the discussion of Section 2.1. The compatibility equation introduced in the continuum case has a natural counterpart in the discretized version. Since one has access to the differences between $\ln(1-D)$ defined at neighboring elements, the summation of these differences along any closed loop (*e.g.,* elementary loops are sufficient) has to be zero. Because of numerical uncertainty, or noise or inappropriate hypotheses on the constitute equations, such sums may significantly differ from 0. First, this property can be used to measure the quality (*i.e.,* consistency) of the approach. Second, it constraints the numerical method used to cope with possible deviations from such compatibility requirements.

The system (18) is over-determined (*e.g.,* for a square mesh made of N elements, the number of equations M is of the order of $4N$, see Section 5). For a structure Ω, the following norm is minimized

$$\mathcal{T} = ||[\boldsymbol{M}]\{\boldsymbol{d}\} - \{\boldsymbol{q}\}||_2^2 \tag{20}$$

with respect to $\{\boldsymbol{d}\}$. A certain robustness can be expected thanks to the redundancy of the equations. This point will be addressed when noise is added to the measurements (see Section 5). The minimization produces the following linear system

$$([\boldsymbol{M}]^t[\boldsymbol{M}])\{\boldsymbol{d}\} = [\boldsymbol{M}]^t\{\boldsymbol{q}\}. \tag{21}$$

A variant to this formulation is to introduce a positive weight matrix $[\boldsymbol{W}]$ to give more importance in the least biased equations. This is equivalent to modifying the norm $||[.]||_2$ and considering the norm $||[.]||_W$. The higher the stress vector, the higher the weight. In the linear system, we suggest to use $[\boldsymbol{W}]$ as a diagonal $M \times M$ matrix

$$[\boldsymbol{W}] = \begin{bmatrix} w_1 & 0 & \dots & 0 \\ 0 & w_2 & \dots & 0 \\ \vdots & \vdots & \ddots & \vdots \\ 0 & 0 & \dots & w_M \end{bmatrix} \tag{22}$$

with

$$w_k = |\bar{g}_k(\{\boldsymbol{u}_m^-\}) + \breve{g}_k(\{\boldsymbol{u}_m^+\})|^\alpha. \tag{23}$$

The power α is adjusted so that the test cases with known damage distributions lead to the best results [23]. A value $\alpha = 1.5$ has been obtained. The system to solve becomes

$$([\boldsymbol{M}]^t[\boldsymbol{W}][\boldsymbol{M}])\{\boldsymbol{d}\} = ([\boldsymbol{M}]^t[\boldsymbol{W}])\{\boldsymbol{q}\}. \tag{24}$$

For Eqn. (24), the matrix $[\boldsymbol{M}]^t[\boldsymbol{W}][\boldsymbol{M}]$ has a zero eigen value and a corresponding eigen vector $\{\boldsymbol{d}\}^t = \{1\ 1\ \dots\ 1\}$ (*i.e.,* this corresponds to a global rescaling of the local elastic constants, or the $(1 - D)$ field, by a fixed multiplicative factor which does not affect the solution). Consequently, one can arbitrarily set one damage component of $\{\boldsymbol{d}\}$. For simplicity, let us choose the i_0^{th} component and consider the following initial condition

$$\{\boldsymbol{d}\}_0^t = \{0\,0\ \dots\ 0\ \ln(1-D)_{i_0}\ 0\ \dots\ 0\} \tag{25}$$

and

$$\{\boldsymbol{\delta}\} = \{\boldsymbol{d}\} - \{\boldsymbol{d}\}_0, \tag{26}$$

one needs to solve over the $(N-1)$ degrees of freedom of $\boldsymbol{\delta}$, $i = 1, ..., N$ and $i \neq i_0$. This corresponds to omitting the i_0^{th} line and column of the $[\boldsymbol{M}]^t[\boldsymbol{W}][\boldsymbol{M}]$ matrix. It is easy to see from Eqn. (4) that the zero-eigenvalue is unique, and thus the resulting matrix is now positive definite

$$([\boldsymbol{M}]^t[\boldsymbol{W}][\boldsymbol{M}])\{\boldsymbol{\delta}\} = ([\boldsymbol{M}]^t[\boldsymbol{W}])\{\boldsymbol{q}\} - ([\boldsymbol{M}]^t[\boldsymbol{W}][\boldsymbol{M}])\{\boldsymbol{d}\}_0. \tag{27}$$

This linear system can be solved by using different numerical methods. A conjugate gradient technique [24] making use of the sparseness of the matrix $([\boldsymbol{M}]^t[\boldsymbol{W}][\boldsymbol{M}])$ is used in all the following applications.

4. ERROR INDICATORS

Different error indicators are now introduced. One of them, which is an error estimator, can be used when the exact solution is known. The other ones can be utilized wether the exact solution is known or not. When the damage field is known, the global quality of the identification can be assessed by using the error estimator η

$$\eta^2 = \frac{1}{N}\sum_{e=1}^{N} \eta_e^2, \tag{28}$$

with

$$\eta_e^2 = \left[\frac{(1-D_e)_{\text{id}}}{(1-D_e)_{\text{pre}}} - 1\right]^2, \tag{29}$$

where the subscript $_{\text{pre}}$ denotes a prescribed quantity and $_{\text{id}}$ an identified one, and N the number of unknowns. For this estimator, the average value $(1-D_e)_{\text{id}}$ is renormalized to obtain a unit average ratio $(1-D_e)_{\text{id}}/(1-D_e)_{\text{pre}}$; this is possible since the identification is

obtained up to a multiplicative constant. From Eqn. (15), an error indicator can be defined when the exact solution is unknown

$$\kappa^2 = \|[\boldsymbol{G}]\{\boldsymbol{D}\} - \{\boldsymbol{g}\}\|_2^2 = \frac{1}{M}\sum_{k=1}^{M} F_r^2(k), \tag{30}$$

where F_r corresponds to the residual associated with the k^{th} equilibrium condition, and M the number of middle nodes. The quantity κ characterizes the average equilibrium residuals. From this point of view, it is close to the indicator based on equilibrium residuals used to assess the quality of a FE computation [25, 26, 27]. This value can be compared to the configuration with a homogeneous damage distribution. The corresponding value, κ_0, is defined when $\{\boldsymbol{D}\}_0^t = \{1\,1\,\ldots\,1\}$

$$\kappa_0^2 = \|[\boldsymbol{G}]\{\boldsymbol{D}\}_0 - \{\boldsymbol{g}\}\|_2^2 = \frac{1}{M}\sum_{k=1}^{M} F_{r0}^2(k), \tag{31}$$

where F_{r0} corresponds to the residual associated with the k^{th} equilibrium condition for a homogeneous distribution of damage. A local indicator can also be defined

$$\kappa_e^2 = \frac{F_{re}^2}{N\kappa^2} \quad \text{with} \quad F_{re}^2 = \sum_{n=1}^{n_m} \frac{F_r^2(n)}{2} \tag{32}$$

so that $\sum_{k=1}^{N} \kappa_e^2(k) = 1$ [since $N\kappa^2 = \sum_{k=1}^{N} F_{re}^2(k)$], where κ_e measures the contribution of each element e to the global quantity κ, and n_m the number of middle points for the considered element e (*i.e.,* generally 4 for an inner element, 3 for edge elements and 2 for corner elements, since the boundary conditions in terms of load are not accounted for). The factor 1/2 is put to equally assign the residual to the two considered elements.

From their definition, the κ and κ_0 indicators correspond to a well-defined physical object, with a continuum limit which quantifies the violation of equilibrium (*i.e.,* integral of the residual volume force density which has to be applied to restore the force balance as shown in Section 2.1). When κ is equal to 0, the exact solution is found. However, a simple dimensional analysis shows that these quantities depend on the stress scale, which is exogenous to the present problem (*i.e.,* based solely on kinematic measurements). Therefore, even though the

solution is defined up to a constant scale factor in $(1-D)$, κ *does* depend on that factor. Consequently, the absolute scale for κ is meaningless. Only relative values can be utilized. However, because of the previous stress scale sensitivity, it is of interest to introduce another quantification of the suitability of a numerical solution to the posed problem. (Note however, that the distinction between two contributions to a global error is not discussed, namely, i) one coming from the possible inconsistency of the input displacement field [*i.e.,* violation of Eqn. (5)] and ii) the numerical quality of the solution assuming no inconsistency.) Associated to the n^{th} middle node where the residual force is $\boldsymbol{F}_r$, the associated work W_r is defined as

$$W_r(D_e^-, D_e^+, \{\tilde{\boldsymbol{u}}_m^-\}, \{\tilde{\boldsymbol{u}}_m^+\}) = |\boldsymbol{F}_r(D_e^-, D_e^+, \{\tilde{\boldsymbol{u}}_m^-\}, \{\tilde{\boldsymbol{u}}_m^+\}).\tilde{\boldsymbol{u}}_{m\pm}| \tag{33}$$

where the displacements $\tilde{\boldsymbol{u}}_{m\pm}, \{\tilde{\boldsymbol{u}}_m^-\}, \{\tilde{\boldsymbol{u}}_m^+\}$ are the measured displacements from which the rigid body motion of elements '$-$' and '$+$' has been removed. This filtering is important to guarantee the objectivity of the indicator W_r. As a practical way of removing the rigid body motion of the two elements '+' and '-', a least squares regression is performed over the twelve nodes surrounding the considered '$\pm$' middle node. If the measured displacement field is strain-free, then $\tilde{\boldsymbol{u}}_{m\pm} = \boldsymbol{0}$. The magnitude of W_r can be compared to the elastic energy $E_{m\pm}$ in the two considered elements '$-$' and '$+$' so that the following local indicator θ no longer depends on the unknown stress scale

$$\theta = \frac{W_r(D_e^-, D_e^+, \{\tilde{\boldsymbol{u}}_m^-\}, \{\tilde{\boldsymbol{u}}_m^+\})}{E_{m\pm}(D_e^-, D_e^+, \{\tilde{\boldsymbol{u}}_m^-\}, \{\tilde{\boldsymbol{u}}_m^+\})}. \tag{34}$$

An error per element can be defined as

$$\theta_e = \sum_{n=1}^{n_m} \frac{\theta(n)}{2}. \tag{35}$$

Again, the factor $1/2$ is put to equally assign the residual to the two considered elements. The global integration over the entire mesh gives an average error indicator

$$\langle\theta\rangle = \frac{1}{M}\sum_{m=1}^{M}\theta(m). \tag{36}$$

Similarly, a global indicator Θ can also be defined as

$$\Theta = \frac{W_r}{E_m}, \tag{37}$$

where W_r is the total work done by the residuals and E_m is the corresponding total elastic energy. The two last indicators are *independent* of the stress scale factor. The above "error" indicators are two examples of an infinite family of similar quantities based on the local density $\theta(m)$, integrated over the considered domain with a measure $\omega(m)$ based on the local elastic energy density, as a homogeneous function of degree 0. Either $\omega(m) = ME_{m\pm}(D_e^-, D_e^+, \{\tilde{\boldsymbol{u}}_m^-\}, \{\tilde{\boldsymbol{u}}_m^+\})/E_m$ and one recovers Θ, or $\omega(m) = 1$ gives $\langle\theta\rangle$. The first weight allows one to give less importance to regions of space where the stress level is low (*i.e.,* more sensitive to measurement uncertainties) and therefore where identification is less secure.

5. APPLICATIONS WITH "FE MEASURES"

A first series of computations considers a squared structure discretized with $a \times a$ quadratic elements. Three edges are clamped and, in the middle of the fourth one, a point-force is applied (Fig. 1-a). Three types of cases are considered. First, no damage at all exists (*i.e.,* it will be referred to as homogeneous, abbreviation h). Second, a layered configuration is analyzed in which the damage field only depends on y (abbreviation l). Third, a random configuration (abbreviation r) with horizontal and vertical damage fluctuations. A uniform damage distribution is chosen and varies between 0 and 0.9 (Fig. 1-b). Each configuration to be studied is identified by three parameters $a-b-$abbreviation$(h, r,$ or $l)$, where b^2 denotes the number of elements with a constant value of damage in a random configuration (r), and $a \times b$ for a layered configuration (l). In the following examples, the first step consists in running a conventional FE analysis. The nodal displacements (*i.e.,* the "measurements") are stored and constitute the inputs to the damage identification procedure. The aim is to use the non-standard FE formulation to recover the damage field.

The structure has $2a(a-1)$ interior middle nodes and a^2 damage unknowns. The conjugate

gradient technique is well-adapted for systems with large dimensions [24]. In the present case, the number of iterations was chosen such that a criterion based on dimensionless residuals is less than 10^{-15} (Fig. 2). Figure 3 compares the damage field used to get the "measurements" and that obtained by the identification procedure for a $10-1-l$ configuration. In the initial determination of the displacement field the prescribed damage field is layered. However, this information is not imposed when the identification analysis is performed. We assume a priori that the damage parameter may take a different value for each element. Yet the layering is very accurately recovered. The error field η_e is also shown in Fig. 3. The estimator is less than 2% and the global value η is equal to 0.6%.

Figure 4 compares a prescribed damage field to a computed one when the damage parameter is constant over 7×7 elements (*i.e.*, $49-7-r$ configuration). This information is not imposed in the analysis. A complete 49×49 field of damage is searched for, and yet the macroscopic checkerboard is obtained with a good accuracy. The only location where the results are less accurate is close to the point where the force is applied thereby leading to a singularity that is not fully captured with the regular mesh used in the simulations. The choice of the point where a non-zero value of D is applied is arbitrary. Different points have been tested and a very weak influence on the error η was found. Furthermore, in Fig. 5, the three error fields η_e, κ_e and θ_e are compared. The three quantities lead to similar results in terms of distribution. This constitutes a validation of the error estimators κ_e and θ_e when the solution is unknown (see following section).

One can note in Fig. 6 that the computed damage field is close to the prescribed values with a random distribution (*i.e.*, $49-1-r$ configuration). The only deviation is obtained close to the point force location where it is known that the "measurements" themselves are not accurate. In this extreme random case the global error η is equal to 3.2%. The results obtained for more than $2a^2$ iterations in the conjugate gradient calculations require less than one minute on a Pentium III PC.

In Table I, a first series of results is given for one realization of the damage fields. In all cases, the error η remains equal to at most few percents, even though the complexity of the problem

is multiplied by 24 for the random configuration $49-1-r$ when compared to $10-1-r$. No significant degradation of the error is noted as the size of the problem increases. A second series of results corresponds to 10 realizations per studied configuration. The average error $\langle\eta\rangle$ remains close to the reference series. These results show that the average error is still of the order of a few percents. To characterize the sensitivity to a measurement noise, a white noise is added to the "measured" displacements (*i.e.,* they contain modes at the scale of the heterogeneities). For a noise amplitude on the displacement field corresponding to a strain variation equal to 10% of the average strain in the structure, the average error $\overline{\eta}$ for 100 realizations is given in Table I. One may note that the order of magnitude is similar to that obtained in the reference configurations with no noise. The robustness of the technique has therefore been demonstrated for homogeneous, layered and random damage fields.

Moreover, the ratio κ/κ_0 is given in Table II. The lower the ratio, the more heterogeneous the damage field, *i.e.,* for the same structure

$$\left(\frac{\kappa}{\kappa_0}\right)_{\text{homogeneous}} \geq \left(\frac{\kappa}{\kappa_0}\right)_{\text{layered}} \geq \left(\frac{\kappa}{\kappa_0}\right)_{\text{random}} . \tag{38}$$

In Table II, the values of the two indicators $\langle\theta\rangle$ and Θ are also reported. It can be mentioned that Θ is greater than $\langle\theta\rangle$ for a given configuration. The order of magnitude of the two indicators is the same when the series with 100 and 2401 elements are analyzed. As already noted, when the number of elements (*i.e.,* unknowns) increases, the values of all the error indicators increases too, but not as fast as the number of unknowns.

6. ANALYSIS OF A BIAXIAL EXPERIMENT ON A COMPOSITE MATERIAL

In this section actual displacement measurements are used. The studied material is a vinylester matrix reinforced by E glass fibers. A quasi-uniform distribution of orientations leads to an isotropic elastic behavior prior to matrix cracking and fiber breakage, which are the main damage mechanisms [28]. A cross-shaped specimen is loaded in a multiaxial testing machine (Fig. 7-a). The experiment is performed in such a way that the forces applied along two

perpendicular directions are identical. By construction of the machine, the specimen center is motionless, thereby avoiding spurious loads.

The displacements fields of Fig. 7-b are measured by digital image correlation [29]. Each "measurement point" corresponds to the center of an interrogation window of size 64×64 pixels, equivalent to a surface of about 8 mm^2. At this scale, the material is not homogeneous (see Fig. 7-a). The shift between two neighboring measurement points is 32 pixels. A sub-pixel algorithm is used. It enables for a displacement resolution of a few hundreds of one pixel for 8-bit pictures [30, 6]. To achieve a better robustness, an iterative and multi-scale version was used [29, 31].

Figure 8 shows four damage fields computed from the measured displacement fields. From the analysis of Fig. 7-b, a crack clearly appears on the top left corner for the last load level before failure. This crack can be observed on the last damage map by the three dark elements. On the two first load levels, one can note at least three different corners where the damage value becomes significant. At this stage, crack inception is likely to have occurred in these three corners. One of them subsequently became preeminent as can be seen on the third load level. This type of analysis cannot be performed by only looking at the displacement field measurements. It shows that the present approach is able to give additional ways of analyzing experimental measurements.

In Fig. 8, the error indicators κ_e and θ_e maps are also plotted for the four different load levels. For the last load level, the errors become significantly altered in the vicinity of the macrocrack, thereby indicating that the equilibrium conditions are no longer satisfied for a discretized, yet continuous displacement field. This is important to note since a "continuum" approach is used even in this extreme case. In the following analysis, the global error indicators κ, κ_0, and Θ are used. Since the damage field is normalized in the same way during the whole sequence, the error levels κ and κ_0 can be compared during the history of loading. Figure 9-a shows their change with the load level. The ratio κ/κ_0 remains constant until the last level. This result indicates that the damage heterogeneity does not evolve significantly until the last level. Two different regimes of the error κ are observed: namely, a first gentle increase up to

approximately 9 kN and then a steeper one up to failure. This trend indicates a change that can be attributed to macrocrack initiation. Figure 9-b shows the change of the indicator Θ with the applied load. Up to approximately 9 kN, the quality of the identification is identical. It starts to degrade for 10 kN and strongly changes for 11 kN, thereby indicating that a continuum description is no longer acceptable. These results show that the two sets of error indicators are complementary and yield different information to analyze the experiments reported in the present section.

7. CONCLUSIONS

An identification procedure was developed to identify damage fields by using kinematic fields. A non-standard finite element formulation was derived in which the nodal displacements are known and the elastic properties (or the damage field) are unknown. The latter are assumed to remain uniform over each element, but vary from element to element. When considering quadratic elements and only dealing with middle nodes, a linear system was derived in which the unknown are written in logarithmic form. Error indicators have been introduced to assess the quality of the identification.

When artificial measurements are used, a comparison could be performed with an a priori prescribed damage field. An overall quality on the order of a few percents was achieved in all the configurations tested herein. When some additional noise was considered, the error did not change significantly. The example of a cross-shaped specimen loaded along two perpendicular directions allowed us to analyze the multiple point inception of macrocracks prior to any visible discontinuity on the measured displacement field. In this last case, the error indicators were a useful tool when the actual solution is unknown.

The present method has the advantage of being directly applicable as a post-processor to the current displacement field measurement techniques such as digital image correlation. When coupled with the present analysis based on quadratic finite elements, it constitutes an *integrated* approach to the determination of damage fields from displacement measurements.

It can be noted that up to now, only an isotropic damage description was used. In the future, extension to more complex descriptions will be sought. This work is still in progress.

ACKNOWLEDGEMENT

The biaxial experiment reported herein was performed with the help of Dr. S. Calloch. The authors wish to thank the anonymous reviewer for her/his helpful suggestions.

REFERENCES

1. Y. Berthaud, D. Paraskevas and M. Taroni, edts., *Photomécanique 95*, (GAMAC, Paris (France), 1995).
2. Y. Berthaud, M. Cottron, F. Morestin, P. Moucheront and M. Taroni, edts., *Photomécanique 98*, (GAMAC, Paris (France), 1998).
3. A. Lagarde, edt., Advanced Optical Methods and Applications in Solid Mechanics, in: *Solid Mechanics and its Applications*, (Kluwer, Dordrecht (Pays Bas), 2000), **82**.
4. P. K. Rastogi, edt., Photomechanics, in: *Topics in Applied Physics*, (Springer, Berlin (Germany), 2000), **77**.
5. Y. Berthaud, M. Cottron, J.-C. Dupré, F. Morestin, J.-J. Orteu and V. Valle, edts., *Photomécanique 2001*, (GAMAC, Paris (France), 2001).
6. J. N. Périé, S. Calloch, C. Cluzel and F. Hild, Analysis of a Multiaxial Test on a C/C Composite by Using Digital Image Correlation and a Damage Model, *Exp. Mech.* **42** [3] (2002) 318-328.
7. D. S. Dawicke and M. A. Sutton, CTOA and Crack-Tunneling Measurements in Thin Sheet 2024-T3 Aluminum Alloy, *Exp. Mech.* **34** (1994) 357-368.
8. L. Humbert, V. Valle and M. Cottron, Experimental Determination and Empirical Representation of Out-of-Plane Displacements in a Cracked Elastic Plate Loaded in Mode I, *Int. J. Solids Struct.* **37** (2000) 5493-5504.
9. J. Desrues, J. Lanier and P. Stutz, Localization of the Deformation in Tests on Sand Samples, *Eng. Fract. Mech.* **21** [4] (1985) 251-262.
10. P. Ladevèze, *Comparaison de modèles de milieux continus*, (thèse d'État, Université Paris 6, 1975). See also: P. Ladevèze, *Updating of complex structures models*, (technical report Aérospatiale, les Mureaux (France), **33.11.01.4**, 1983).
11. R. V. Kohn and B. D. Lowe, A Variational Method for Parameter Identification, *Math. Mod. Num. Ana.* **22** [1] (1988) 119-158.
12. H.D. Bui and A. Constantinescu, Spatial localization of the error of constitutive law for the identification of defects in elastic solids, *Arch. Mech.* **52** (2000) 511-522.

13. P. Ladevèze, D. Nedjar and M. Reynier, Updating of Finite Element Models Using Vibration Tests, *AIAA* **32** [7] (1994) 1485-1491.
14. G. Geymonat, F. Hild and S. Pagano, Identification of Elastic Parameters by Displacement Field Measurement, *C. R. Mecanique* **330** (2002) 403-408.
15. S. Calloch, D. Dureisseix and F. Hild, Identification de modèles de comportement de matériaux solides : utilisation d'essais et de calculs, *Technologies et Formations* **100** (2002) 36-41.
16. M. Grédiac, Principe des travaux virtuels et identification, *C. R. Acad Sci. Paris* **309** [Série II] (1989) 1-5.
17. M. Grédiac, E. Toussaint and F. Pierron, L'identification des propriétés mécaniques de matériaux avec la méthode des champs virtuels, une alternative au recalage par éléments finis, *C. R. Mecanique* **330** (2002) 107-112.
18. H. D. Bui, Sur quelques problèmes inverses élastiques en mécanique de l'endommagement, *C. R. 2e Colloque national de calcul des structures*, (Hermès, Paris (France), 1995) **1** 25-35.
19. S. Andrieux, A. Ben Abda and H. D. Bui, Sur l'identification de fissures planes via le concept de réciprocité en élasticité, *C. R. Acad. Sci. Paris* **Série I** [t. 324] (1997) 1431-1438. See also: S. Andrieux, A. Ben Abda and H. D. Bui, Reciprocity principle and crack identification, *Inverse Problems* **15** (1999) 59-65.
20. B. P. Flannery, H. W. Deckman, W. G. Roberge and K. L. D'Amico, Three-Dimensional Microtomography, *Science* **237** (1987) 1439-1444.
21. J. Lemaitre and J.-L. Chaboche, *Mécanique des matériaux solides*, (Dunod, Paris (France), 1985).
22. D. Claire, *Identification de propriétés thermomécaniques résolues spatialement*, (MSc report, ENS de Cachan, 2002).
23. D. Claire, F. Hild and S. Roux, Identification of damage fields using kinematic measurements, *C. R. Mecanique* **330** (2002) 729-734.
24. W. H. Press, S. A. Teukolsky, W. T. Vetterling and B. P. Flannery, *Numerical Recipes in Fortran*, (Cambridge University Press, Cambridge (USA), 1992).
25. I. Babushka and W.C. Rheinboldt, Error Estimates for Adaptive Finite Element Computation, *SIAM J. Anal.* **15** [4] (1978) 736-754.
26. I. Babushka and W.C. Rheinboldt, A posteriori error estimates for the finite element method, *Int. J. Num. Meth. Engng.*, **12** 1597-1615.
27. O.C. Zienkiewicz and R.L. Taylor, Error Estimates and Adaptative Finite Element Refinement, *The Finite Element Method*, **1** fourth edition, (McGraw-Hill, London (UK), 1988), 398-435. See also references therein.
28. F. Collin, Y. Berthaud and F. Hild, Visualisation par analyse d'images de la répartition des déformations et de l'amorçage dans un matériau composite, in: Y. Berthaud, M. Cottron, F. Morestin, P. Moucheront et M. Taroni, edts., *Photomécanique 98*, (GAMAC, Paris (France), 1998), 241-248.
29. F. Hild, CORRELI^{LMT}*: A Software for Displacement Field Measurements by Digital Image Correlation*, (LMT-Cachan, internal report **254**, 2002).
30. F. Hild, J.-N. Périé and M. Coret, *Mesure de champs de déplacements 2D par intercorrélation d'images :*

CORRELI^{2D}, (LMT-Cachan, rapport interne **230**, 1999).

31. F. Hild, B. Raka, M. Baudequin, S. Roux and F. Cantelaube, Multi-Scale Displacement Field Measurements of Compressed Mineral Wool Samples by Digital Image Correlation, *Appl. Optics* **IP 41** (2002) 6815-6828.

APPENDIX

For a quadratic square element (*i.e.*, with 8 displacement nodes), the strain energy is computed for two neighboring elements. The sum of two energies is differentiated with respect to the corresponding degrees of freedom so that two equations are obtained per considered middle node. The equilibrium equation can be written as

$$\bar{g}(\{\boldsymbol{u}_e^-\})(1-D_e^-) = \breve{g}(\{\boldsymbol{u}_e^+\})(1-D_e^+) \tag{39}$$

where the superscript $^-$ corresponds to quantities relative to one element and $^+$ to the other one. Only two different situations arise, namely, a vertical or a horizontal boundary. For a vertical boundary, the projection of the equilibrium equation along the $\boldsymbol{e}_x$ direction yields

$$\begin{aligned}
\bar{g}(\{\boldsymbol{u}_e^-\}) &= \frac{u_1^- - u_3^- - 8u_4^- - u_5^- + u_7^- + 8u_8^-}{15} \\
&+ \frac{v_1^- + 4v_2^- + v_3^- - v_5^- - 4v_6^- - v_7^-}{9} \\
&+ \frac{1-\nu_0}{2\nu_0}\left(\frac{-34u_1^- - 26u_3^- - 8u_4^- - 26u_5^- - 34u_7^- + 128u_8^-}{45}\right. \\
&+ \left.\frac{-5v_1^- + 4v_2^- + v_3^- - v_5^- - 4v_6^- + 5v_7^-}{9}\right)
\end{aligned} \tag{40}$$

and

$$\begin{aligned}
\breve{g}(\{\boldsymbol{u}_e^+\}) &= \frac{-u_1^+ + u_3^+ + 8u_4^+ + u_5^+ - u_7^+ - 8u_8^+}{15} \\
&+ \frac{-v_1^+ - 4v_2^+ - v_3^+ + v_5^+ + 4v_6^+ + v_7^+}{9} \\
&+ \frac{1-\nu_0}{2\nu_0}\left(\frac{-26u_1^+ - 34u_3^+ + 128u_4^+ - 34u_5^+ - 26u_7^+ - 8u_8^+}{45}\right. \\
&+ \left.\frac{-v_1^+ - 4v_2^+ + 5v_3^+ - 5v_5^+ + 4v_6^+ + v_7^+}{9}\right)
\end{aligned} \tag{41}$$

by using the numbering i given in Fig. A1. Similarly, the projection along the $\boldsymbol{e}_y$ direction yields

$$\begin{aligned}
\bar{g}(\{\boldsymbol{u}_e^-\}) &= \frac{-5u_1^- + 4u_2^- + u_3^- - u_5^- - 4u_6^- + 5u_7^-}{9} \\
&+ \frac{-8v_1^- - 4v_3^- + 8v_4^- - 4v_5^- - 8v_7^- + 16v_8^-}{9} \\
&+ \frac{1-\nu_0}{2\nu_0}\left(\frac{u_1^- + 4u_2^- + u_3^- - u_5^- - 4u_6^- - u_7^-}{9}\right. \\
&+ \left.\frac{-77v_1^- - 43v_3^- + 56v_4^- - 43v_5^- - 77v_7^- + 184v_8^-}{4}\right)
\end{aligned} \tag{42}$$

and

$$\begin{aligned}\breve{g}(\{\boldsymbol{u}_e^+\}) &= \frac{-u_1^+ - 4u_2^+ + 5u_3^+ - 5u_5^+ + 4u_6^+ + u_7^+}{9} \\ &+ \frac{-4v_1^+ - 8v_3^+ + 16v_4^+ - 8v_5^+ - 4v_7^+ + 8v_8^+}{9} \\ &+ \frac{1-\nu_0}{2\nu_0}\left(\frac{-u_1^+ - 4u_2^+ - u_3^+ + u_5^+ + 4u_6^+ + u_7^+}{9}\right. \\ &+ \left.\frac{-43v_1^+ - 77v_3^+ + 184v_4^+ - 77v_5^+ - 43v_7^+ + 56v_8^+}{4}\right) \end{aligned} \tag{43}$$

For a horizontal boundary, the projection along the $\boldsymbol{e}_x$ direction yields

$$\begin{aligned}\bar{g}(\{\boldsymbol{u}_e^-\}) &= \frac{-8u_1^- + 16u_2^- - 8u_3^- - 4u_5^- + 8u_6^- - 4u_7^-}{9} \\ &+ \frac{-5v_1^- + 5v_3^- - 4v_4^- - v_5^- + v_7^- + 4v_8^-}{9} \\ &+ \frac{1-\nu_0}{2\nu_0}\left(\frac{-77u_1^- + 184u_2^- - 77u_3^- - 43u_5^- + 56u_6^- - 43u_7^-}{45}\right. \\ &+ \left.\frac{v_1^- - v_3^- - 4v_4^- - v_5^- + v_7^- + 4v_8^-}{4}\right) \end{aligned} \tag{44}$$

and

$$\begin{aligned}\breve{g}(\{\boldsymbol{u}_e^+\}) &= \frac{-4u_1^+ + 8u_2^+ - 4u_3^+ - 8u_5^+ + 16u_6^+ - 8u_7^+}{9} \\ &+ \frac{-v_1^+ + v_3^+ + 4v_4^+ - 5v_5^+ + 5v_7^+ - 4v_8^+}{9} \\ &+ \frac{1-\nu_0}{2\nu_0}\left(\frac{-43u_1^+ + 56u_2^+ - 43u_3^+ - 77u_5^+ + 184u_6^+ - 77u_7^+}{45}\right. \\ &+ \left.\frac{-v_1^+ + v_3^+ + 4v_4^+ + v_5^+ - v_7^+ - 4v_8^+}{9}\right) \end{aligned} \tag{45}$$

and the projection along the $\boldsymbol{e}_y$ direction yields

$$\begin{aligned}\bar{g}(\{\boldsymbol{u}_e^-\}) &= \frac{u_1^- - u_3^- - 4u_4^- - u_5^- + u_7^- + 4u_8^-}{9} \\ &+ \frac{v_1^- + 8v_2^- + v_3^- - v_5^- - 8v_6^- - v_7^-}{15} \\ &+ \frac{1-\nu_0}{2\nu_0}\left(\frac{-5u_1^- + 5u_3^- - 4u_4^- - u_5^- + u_7^- + 4u_8^-}{9}\right. \\ &+ \left.\frac{-34v_1^- + 128v_2^- - 34v_3^- - 26v_5^- - 8v_6^- - 26v_7^-}{45}\right) \end{aligned} \tag{46}$$

and

$$
\begin{aligned}
\breve{g}(\{\boldsymbol{u}_e^+\}) &= \frac{-u_1^+ + u_3^+ + 4u_4^+ + u_5^+ - u_7^+ - 4u_8^+}{9} \\
&+ \frac{-v_1^+ - 8v_2^+ - v_3^+ + v_5^+ + 8v_6^+ + v_7^+}{15} \\
&+ \frac{1-\nu_0}{2\nu_0}\left(\frac{-u_1^+ + u_3^+ + 4u_4^+ - 5u_5^+ + 5u_7^+ - 4u_8^+}{9}\right. \\
&+ \left.\frac{-26v_1^+ - 8v_2^+ - 26v_3^+ - 34v_5^+ + 128v_6^+ - 34v_7^+}{45}\right)
\end{aligned}
\tag{47}
$$

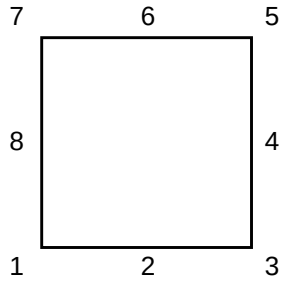

Figure A1. Node numbering of a quadratic element.

List of Tables

Table I. Errors η for different configurations, $\langle\eta\rangle$ when 10 random selections are performed per configuration, $\overline{\eta}$ when noise is added (100 random selections are sampled per configuration).

Configuration	$10-1-h$	$10-1-l$	$10-1-r$	$49-1-h$	$49-1-l$	$49-1-r$
η	0.002	0.006	0.013	0.017	$0.024^{(1)}$	$0.032^{(1)}$
$\langle\eta\rangle$	–	0.007	0.007	–	0.023	0.039
$\overline{\eta}$	0.015	0.016	0.026	0.020	0.032	0.051

$^{(1)}$configurations of Fig. 1-b.

Table II. Ratio κ/κ_0, error indicators $\langle\theta\rangle$ and Θ for different types of configurations.

Configuration	10-1-h	10-1-l	10-1-r	49-1-h	49-1-l[(1)]	49-1-r[(1)]
κ/κ_0	0.86	3.4×10^{-3}	2.2×10^{-3}	0.77	1.0×10^{-2}	4.7×10^{-3}
$\langle\theta\rangle$	1.5×10^{-4}	3.3×10^{-4}	2.7×10^{-4}	6.4×10^{-4}	1.3×10^{-3}	1.6×10^{-3}
Θ	2.0×10^{-3}	1.4×10^{-3}	1.6×10^{-3}	6.3×10^{-3}	7.4×10^{-3}	4.5×10^{-3}

[(1)]configurations of Fig. 1-b.

List of Figures

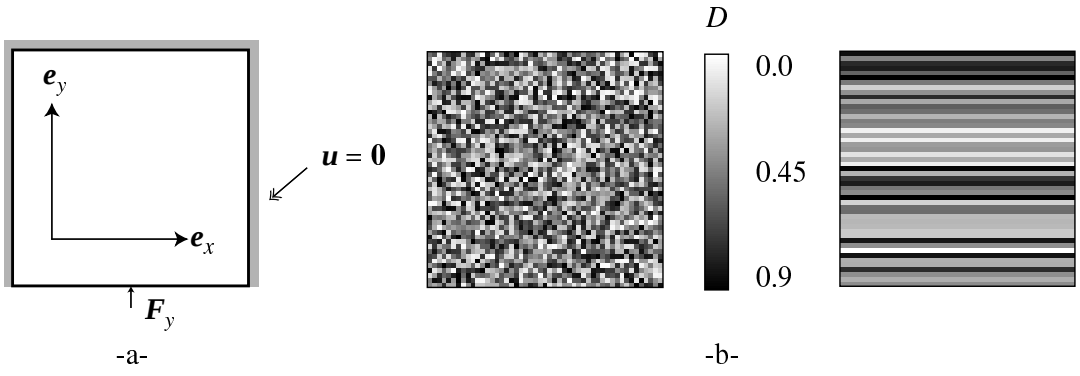

Figure 1. a-Considered structure. In the middle of one edge a point force $\boldsymbol{F}_y$ is applied. b-Random ($49-1-r$ configuration) or layered ($49-1-l$ configuration) damage field D.

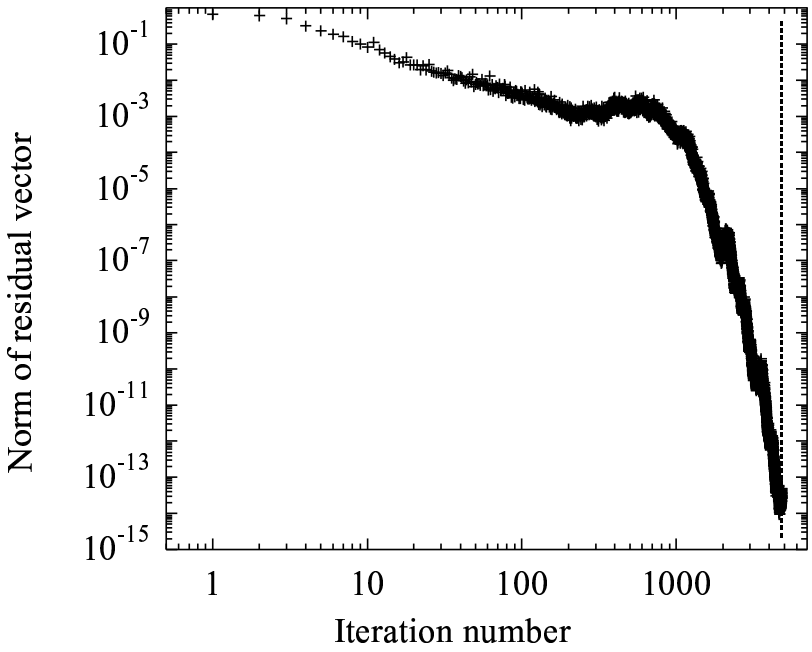

Figure 2. Norm of residual vector associated with the conjugate gradient technique versus iteration number ($49-1-l$ configuration).

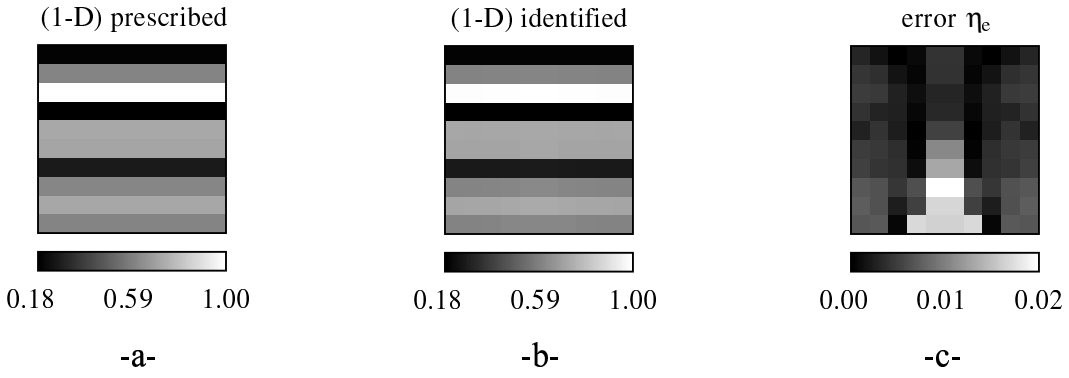

Figure 3. Prescribed (a) and identified (b) damage fields for a $10-1-r$ configuration. Corresponding error field (c) η_e.

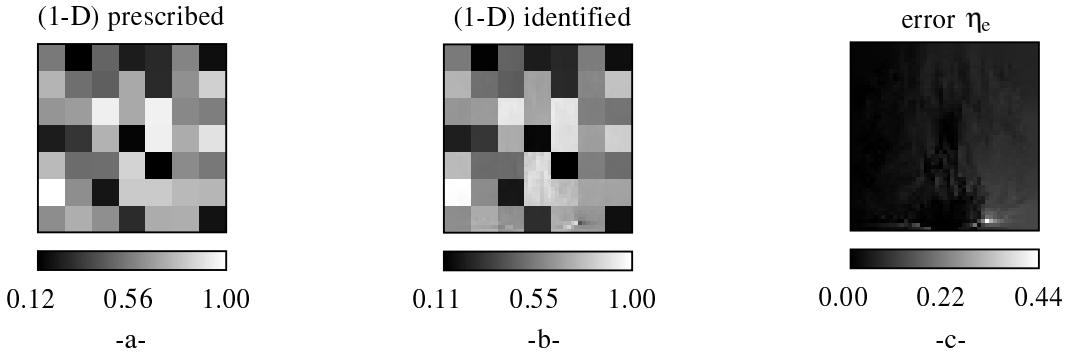

Figure 4. Prescribed (a) and identified (b) damage fields for a $49-7-r$ configuration. Corresponding error field (c) η_e.

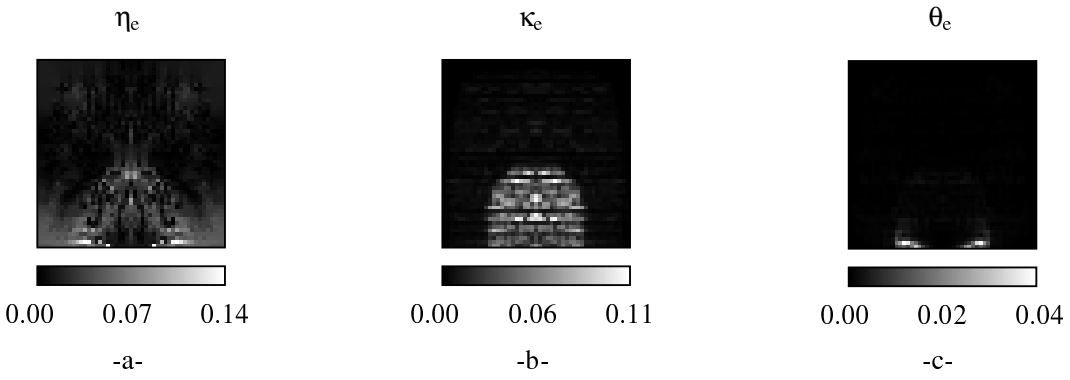

Figure 5. Error maps η_e, κ_e and θ_e for a $49 - 1 - l$ configuration.

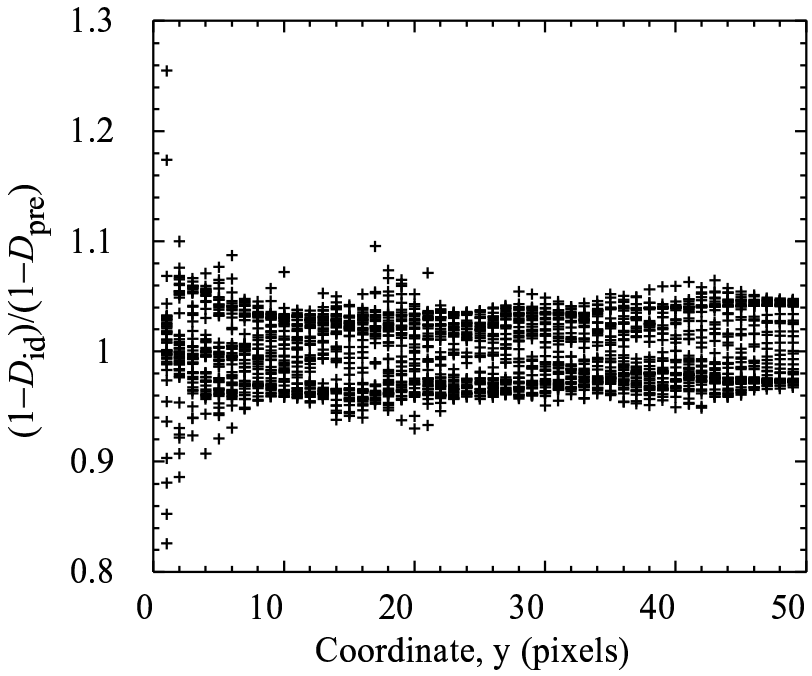

Figure 6. Ratio of identified to prescribed damage versus ordinate y in a $49-1-r$ configuration.

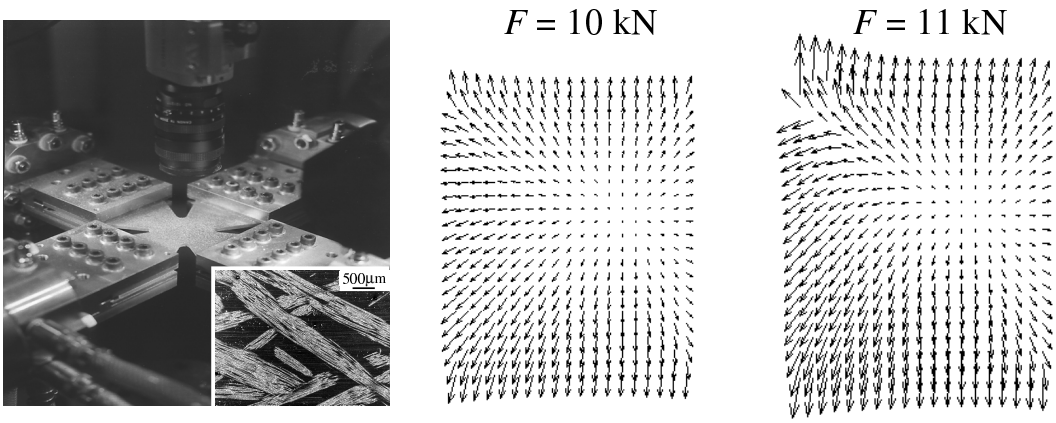

Figure 7. a-Sample in the testing machine ASTRÉE and microstructure of the studied composite. b-Displacement fields measured by digital image correlation for two load levels (failure load: 11.1 kN).

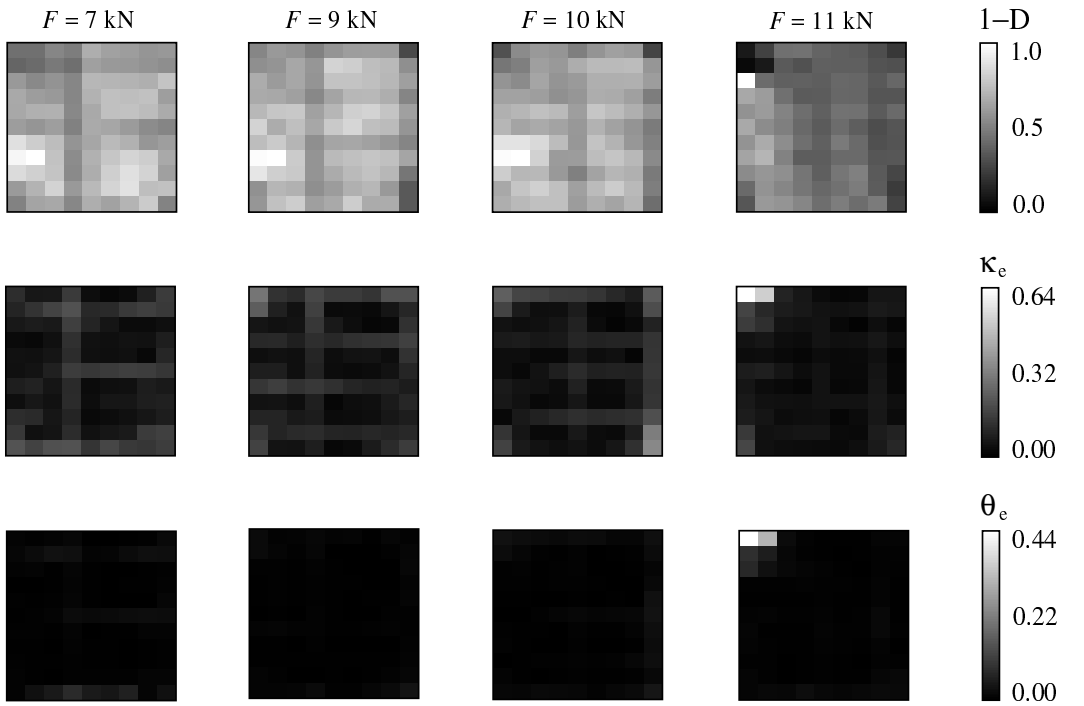

Figure 8. Computed damage fields $(1 - D)$ for 4 load levels and corresponding error fields κ_e and θ_e.

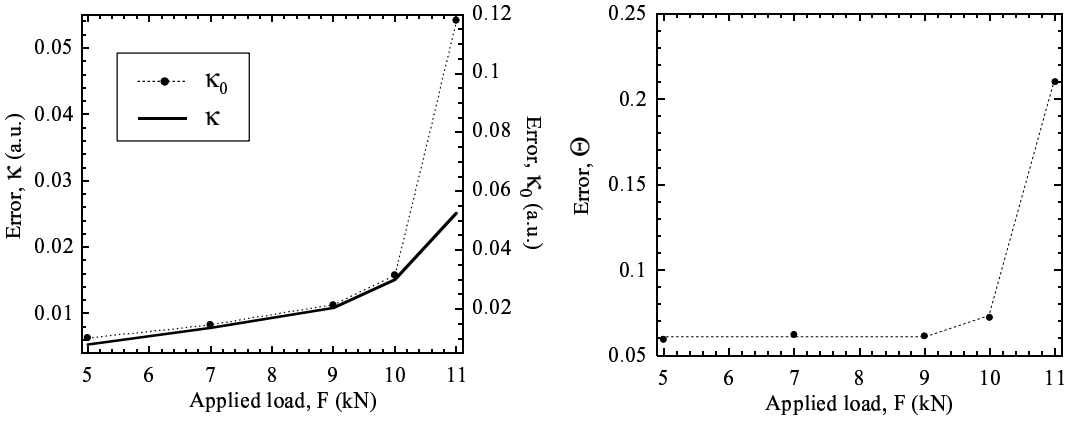

Figure 9. Error indicators κ, κ_0 and Θ versus load level. From the analysis of the results, it is expected that crack initiation occurred around 9 kN.